

Article

Effects of Mullite, Maghemite, and Silver Nanoparticles Incorporated in β -Wollastonite on Tensile Strength, Magnetism, Bioactivity, and Antimicrobial Activity

Hamisah Ismail ^{1,2}, Farah 'Atiqah Abdul Azam ¹, Zalita Zainuddin ¹, Hamidun Bunawan ³ ,
Muhamad Afiq Akbar ³, Hasmaliza Mohamad ² and Muhammad Azmi Abdul Hamid ^{1,*}

¹ School of Applied Physics, Faculty of Science & Technology, Universiti Kebangsaan Malaysia, Bangi 43600, Selangor, Malaysia; hamisahismail@usm.my (H.I.); qfaara@gmail.com (F.'A.A.A.); zazai@ukm.edu.my (Z.Z.)

² School of Materials and Mineral Resources Engineering, Universiti Sains Malaysia, Nibong Tebal 14300, Penang, Malaysia; hasmaliza@usm.my

³ Institute of Systems Biology, Universiti Kebangsaan Malaysia, Bangi 43600, Selangor, Malaysia; hamidun.bunawan@ukm.edu.my (H.B.); muhdafiq.akbar@gmail.com (M.A.A.)

* Correspondence: azmi@ukm.edu.my

Abstract: β -wollastonite (β W) has sparked much interest in bone defect recovery and regeneration. Biomaterial-associated infections and reactions between implants with human cells have become a standard clinical concern. In this study, a green synthesized β W, synthesized from rice husk ash and a calcined limestone precursor, was incorporated with mullite, maghemite, and silver to produce β wollastonite composite (β WMAF) to enhance the tensile strength and antibacterial properties. The addition of mullite to the β WMAF increased the tensile strength compared to β W. In vitro bioactivity, antibacterial efficacy, and physicochemical properties of the β -wollastonite and β WMAF were characterized. β W and β WMAF samples formed apatite spherules when immersed in simulated body fluid (SBF) for 1 day. In conclusion, β WMAF, according to the tensile strength, bioactivity, and antibacterial activity, was observed in this research and appropriate for the reconstruction of cancellous bone defects.

Keywords: β -wollastonite; mullite; maghemite; silver; bioactivity



Citation: Ismail, H.; Azam, F.'A.; Zainuddin, Z.; Bunawan, H.; Akbar, M.A.; Mohamad, H.; Hamid, M.A.A. Effects of Mullite, Maghemite, and Silver Nanoparticles Incorporated in β -Wollastonite on Tensile Strength, Magnetism, Bioactivity, and Antimicrobial Activity. *Materials* **2021**, *14*, 4643. <https://doi.org/10.3390/ma14164643>

Academic Editor: Alina Sionkowska

Received: 1 July 2021

Accepted: 13 August 2021

Published: 18 August 2021

Publisher's Note: MDPI stays neutral with regard to jurisdictional claims in published maps and institutional affiliations.



Copyright: © 2021 by the authors. Licensee MDPI, Basel, Switzerland. This article is an open access article distributed under the terms and conditions of the Creative Commons Attribution (CC BY) license (<https://creativecommons.org/licenses/by/4.0/>).

1. Introduction

At this time, many commercial bone replacements are being used to replace bone implants in orthopedic trauma surgery procedures. However, their widespread application is limited because they do not meet several of the regenerative needs of bone tissue and practical needs related to handling and surgery. There are potential and growing applications of bioactive calcium silicate for commercial bone replacement, such as in dentistry [1], load-bearing [2], and scaffold [3,4], but it has some limitations, such as high brittleness [5], low antibacterial resistance [6], and no magnetic properties [7]. Due to the problems encountered, a dopant material should be added to the bioactive calcium silicate to improve the implant's properties. In the present study, examples of dopant materials were applied in calcium silicate ceramics, such as strontium (Sr) [8], copper (Cu) [9], magnesium (Mg) [10], zirconia (ZrO_2) [10], and titania (TiO_2) [11]. The justification for using these particular metal oxides for doping is that they contain metallic elements that are similar to trace elements found in bone, such as zinc (Zn), magnesium (Mg), and strontium (Sr), all of which have been shown to have potential benefits in encouraging formation bone growth [12]. The use of zirconia and titanium alloys as implantable orthopedic materials in the past refers to the doping of other metal oxides containing zirconium (Zr) [13] and titanium (Ti) [14]. Using metal oxide nanoparticles as a dopant improved antibacterial activity while minimizing toxicity, chemical stability, and thermal resistance.

Iron compound nanoparticles or magnetic nanoparticles have an essential aspect in biomedical engineering and biology. Magnetite (Fe_3O_4) and maghemite ($\gamma\text{-Fe}_2\text{O}_3$), the two typical forms of magnetic nanoparticles, are most suitable in biomedical science and engineering due to their non-toxic property, biocompatibility, high surface to volume ratio, ability to excellently carry a broad range of biological ligands, and existence of natural routes for its degradation [15,16], due to a superior class of metal oxide nanoparticles with unique magnetic properties and more outstanding biocompatibility. Laterally, with the growing uses of magnetic nanoparticles, magnetic nanoparticles' possible toxic effects have been a far-reaching burden [17–20]. Numerous outcomes point out that magnetic nanoparticles suggestively diminish the cell viability of human mesothelioma [21], epithelial cell lines [22], human macrophage [22], and hinder the standard formation of PC12 neuronal cell morphology [23]. In other studies, the dimercaptosuccinic acid (DMSA)-coated MNPs reduce the mitochondrial activity of human fibroblasts at a high concentration of magnetic nanoparticles [17]. However, magnetic nanoparticles' cytotoxicity statistics are challenging since magnetic nanoparticles' toxic effects are influenced by several factors, such as magnetic properties, distribution of size, and surface coating [17]. Therefore, it is critical to select the cell line for the cytotoxicity assessment of precise magnetic nanoparticles. However, the cytotoxicity studies of magnetic nanoparticles incorporated in calcium silicate bioceramics are restricted because the cytotoxicity mechanism is still in early investigation [18].

Currently, antimicrobial activities of the silver ion have been reported against both Gram-positive and Gram-negative bacteria, protozoa, fungi, and certain viruses [19]. Silver ions are widely used to inhibit bacterial growth in various medical utilization, including catheters, dental biomaterials, burn trauma, and surgical appliances [9,19,20,24]. Some researchers have described the deliberate addition of chemical components into biomaterials to gain antimicrobial effects [25,26], and silver is the most generally used because of its excellent antibacterial activity [27,28]. Commonly, silver nanoparticles are less toxic than silver ions [28] and other metals [29]. The doping of the silver, copper, and zinc with hydroxyapatite, which exhibited potential action on *Escherichia coli* (*E. coli*) and *Staphylococcus aureus* (*S. aureus*) microbial growth inhibition, has been widely studied [30–32]. Meanwhile, the consumption of doping antibacterial agents, such as silver nanoparticles [33,34] and copper [35,36] doped in β -wollastonite, is still new to explore. Lohbauer et al. mentioned that approximately one ppm with a consistent release of silver ions has no cytotoxic effect on the viability of human epidermal keratinocytes [37]. Another researcher reported that nanocrystal composite of HA doped Ag exhibited biocompatible or not toxic effects on L929 cells when an up to 2.2 ppm concentration of 50/1000 $\mu\text{g}/\text{mL}$ was applied. Otherwise, for HA/Ag at 197 ppm, cell viability reduced to 40%, showing increased toxicity [38].

This research aims to create a green synthesis of β -wollastonite obtained from rice husk ash and calcined limestone incorporated with mullite, maghemite, and silver nanoparticles to test its tensile strength, magnetic properties, bioactivity, and antibacterial potential.

2. Materials and Methods

The β -wollastonite (βW) was synthesized from agricultural and natural rice husk ash and limestone sources. The silica (SiO_2) source from fired rice husk was obtained from a rice mill industry in Penang, Malaysia. Meanwhile, calcium oxide (CaO) was collected from a nearby limestone quarry in Perak, Malaysia. The β -wollastonite composite (βWMAF) consists of 20 wt.% of mullite, 5 wt.% of maghemite ($\gamma\text{-Fe}_2\text{O}_3$), and 5 wt.% silver (Ag). Mullite was obtained from the calcination of andalusite for 8 h at 1450 °C and collected from a mining quarry in Terengganu, Malaysia. Mullite selection of 20 wt.% refers to a previous study by Farah et al. [39], which found optimum compressive strength was obtained when using 20 wt.%. Silver nanoparticles with a purity of 99% and a particle size of <100 nm were purchased from Sigma-Aldrich (Petaling Jaya, Malaysia). The results were taken from a previous study by Farah et al. [34], which showed optimum results for antibacterial properties when 5 wt.% was used in the previous study. Gram-positive *Staphylococcus aureus* (*S. aureus*) ATCC11632 and Gram-negative *Escherichia coli* (*E. coli*) ATCC10536 were

used for antibacterial activity evaluation in the antibacterial study. A culture agar (nutrient agar 17 g/L from LB, Wako) and a culture broth (Mueller Hinton Broth 21 g/L from LB, Wako) were used as a media cultivation nutrient. The maghemite nanoparticle was self-synthesized using the co-precipitation technique, and the raw materials were used as anhydrous iron (II) chloride (FeCl_2 , 98% purity) and anhydrous iron (III) chloride (FeCl_3 , 97% purity), supplied by Sigma-Aldrich (Petaling Jaya, Malaysia).

2.1. Preparation of βW and βWMAF Disc

A solid-state reaction method assisted by using an autoclave reactor was adopted to prepare β -wollastonite (βW); the $\text{CaO}:\text{SiO}_2$ is 55:45. The CaO and SiO_2 were mixed using deionized water, autoclaved for 8 h at 135 °C, and kept to dry in the oven for 24 h. Afterward, the dried mixture was sintered at 950 °C for 2 h. A brief explanation of the preparation of βW was completed and described in the previous study [40,41].

To produce the βWMAF sample, the mullite powder, maghemite, and silver were milled using ball milling at 250 rpm for 15 min to obtain the homogenous mixture. The βW as a control sample and βWMAF mixture were pressed under 2.5 tons to get a disc (12.0 ± 0.1 mm diameter \times 2.0 ± 0.1 mm thickness).

2.2. Characterization of βW and βWMAF

The phase identification of βW , mullite, maghemite, silver, and βWMAF was detected via X-ray diffraction (XRD, D8 Advance, Bruker, Karlsruhe, Germany) using $\text{Cu K}\alpha$ radiation ($\lambda = 0.15406$ nm) with a step size of $0.025^\circ/\text{step}$, a counting time of 0.1 s, and the Bragg's angle ranging from 20 – 70° . The morphology and elemental analyses were examined using a field emission scanning electron microscope (FESEM, Carl Zeiss, Compact, Jena, Germany) and an energy dispersive (EDS, IncaEnergy, Oxfordshire, UK) spectrometer, and the samples were platinum sputter-coated before analysis. The microscope was operated at a voltage of 3.0 kV.

2.3. Diametral Tensile Strength βW and βWMAF

The diametral compression or Brazilian disc test is an excellent way to measure the tensile strength of brittle materials, such as ceramic and biomaterials [42]. Theory of elasticity, finite element analysis, and photoelasticity studies have all confirmed the state of stress. The resulting findings were curiously consistent and in perfect agreement with Hertz's classical analysis [43]. Except for the immediate vicinity of the loading points, there was a convergence of the stress solutions throughout the disc in all cases. The diametral compression test yielded strength values that were sometimes comparable to flexure strengths but not always [44].

In this experiment, the diametral tensile strength of the βW and βWMAF was evaluated using the Brazilian test, referring to the ASTM C496 standard [39]. The length and diameter of five specimen discs (12.0 ± 0.1 mm in diameter \times 2.0 ± 0.1 mm in thickness) were measured. The sample was positioned between steel platens and tested on a Universal Testing Machine (Instron 8874, Instron, Norwood, MA, United States) with the load cell 5 kN and a loading rate of 0.1 mm/min [39]. The maximum compression load at failure was calculated from the load-deflection curves identified. The tensile stress here is directly proportional to the applied compressive load. Using the following relationship, the strength value of the βW and βWMAF samples was determined: diametral tensile strength, $\sigma_t = 2P/\pi DT$, where P is the peak load (N), D is the diameter (mm), and T is the sample thickness (mm).

2.4. Magnetic Properties

Magnetic properties were evaluated using a vibrating sample magnetometer (VSM, Lakeshore 7410, Lake Shore Cryotronics, Inc., Westerville, OH, United States) with an applied magnetic field of 14 k Oe at room temperature for maghemite ($\gamma\text{-Fe}_2\text{O}_3$) βW and βWMAF powders. The external magnetic field vibration could be applied both in the

transverse and longitudinal directions of the vibration. Each sample's magnetic moment was measured over a range of magnetic fields applied between -1.4×10^3 and 1.4×10^3 Oe with a 0.1 emu sensitivity.

2.5. In-Vitro Bioactivity

The ability to form apatite on the surface of the β W and β WMAF discs was tested using an SBF solution whose ionic composition is similar to that of human physiological body fluid. Generally, β W and β WMAF discs were soaked in 30 mL of SBF solution for 1, 7, and 14 days in a polyethylene bottle and retained in an incubator at 37 °C, referring to the procedure by Kokubo and Takadama [45]. Every three days, the SBF solution was replaced. After soaking each day, the β W and β WMAF discs were removed from the SBF solution, immersed in acetone for 2 h, washed three times with deionized water, and dried in the incubator. The SBF solutions' pH values were measured after 1, 7, and 14 days of soaking β W and β WMAF discs. Phase, functional group, morphology observation, and elemental composition were used to determine the apatite formation on β W and β WMAF disc surfaces.

2.6. Ca, P, Fe, and Ag Release in SBF Solution

To evaluate the ion dissolution from β W and β WMAF discs, the SBF was prepared according to Kokubo's method [45]. The β W and β -WMAF discs were put in a 30 mL polyethylene bottle immersed in SBF solutions at 36.5 °C in an incubator for 1, 7, and 14 days without changing the solution. The concentrations of Si, Ca, P, Fe, and Ag ions in the SBF solutions were calculated by an inductively coupled plasma mass spectrometer (ICP-MS, Perkin Elmer, Waltham, MA, United State).

2.7. Antimicrobial Activity

Using *Escherichia coli* ATCC10536 and *Staphylococcus aureus* ATCC11632, the antimicrobial activity was carried out using a disc diffusion method using Mueller Hinton Agar (MHA). All the specimens and apparatus were sterilized in an autoclave at 121 °C for 15 min), and all the tasks were inside the laminar airflow chamber. The bacteria cultures were prepared in nutrient broth (Difco 234000, Nelson-Jameson, Marshfield, WI, USA) at a concentration of $\sim 1.5 \times 10^8$ CFU/mL corresponding to the density of 0.5 MacFarland. Next, under sterilized conditions, *E. coli* and *S. aureus* cultures were swabbed on the agar petri dish using a sterile cotton swab. The β WMAF disc was placed on the agar, followed by the β W disc as negative control and Ag disc as a positive control. These petri discs were incubated at 37 °C for 24 h. Subsequently, the zone of inhibition (ZOI) was calculated in millimeters (mm) for duplicate specimens for each sample.

2.8. Statistical Analyses

The bioactivity test, magnetization test, antibacterial test, and five samples for diametral tensile strength were duplicated. For $n = 2$ and 5, all data were expressed as means and standard deviations.

3. Results and Discussion

3.1. Characterization of β W and β WMAF

Figure 1 exhibits XRD analysis of all the raw materials: (a) maghemite (γ -Fe₂O₃), (b) mullite, (c) silver, (d) β W, and (e) β WMAF powders. The prominent peak of each raw material was an exhibit at β WMAF (Figure 1e). The prominent peak of maghemite (γ -Fe₂O₃) phase was observed at theta 35°, for mullite at 26.1°, silver (Ag) clearly at 38.2°, and most of the peak of β WMAF was dominant by β -wollastonite phase (β -CaSiO₃) at 30°, 50.2°, 53.3°, and 39.1°. Referring to previous reports, amorphous CaSiO₃ has a faster apatite-formation capacity owing to the accelerated release of Ca ions relative to alpha-wollastonite (α -CaSiO₃) and beta-wollastonite (β -CaSiO₃) [46]. Consequently, β WMAF materials may enhance bioactivity. For reference, the patterns of maghemite (ICDD no:

39-1346), mullite (ICDD no: 74-4144), silver (ICDD no: 04-0783), and β -wollastonite (ICDD no: 043-1460) are referred.

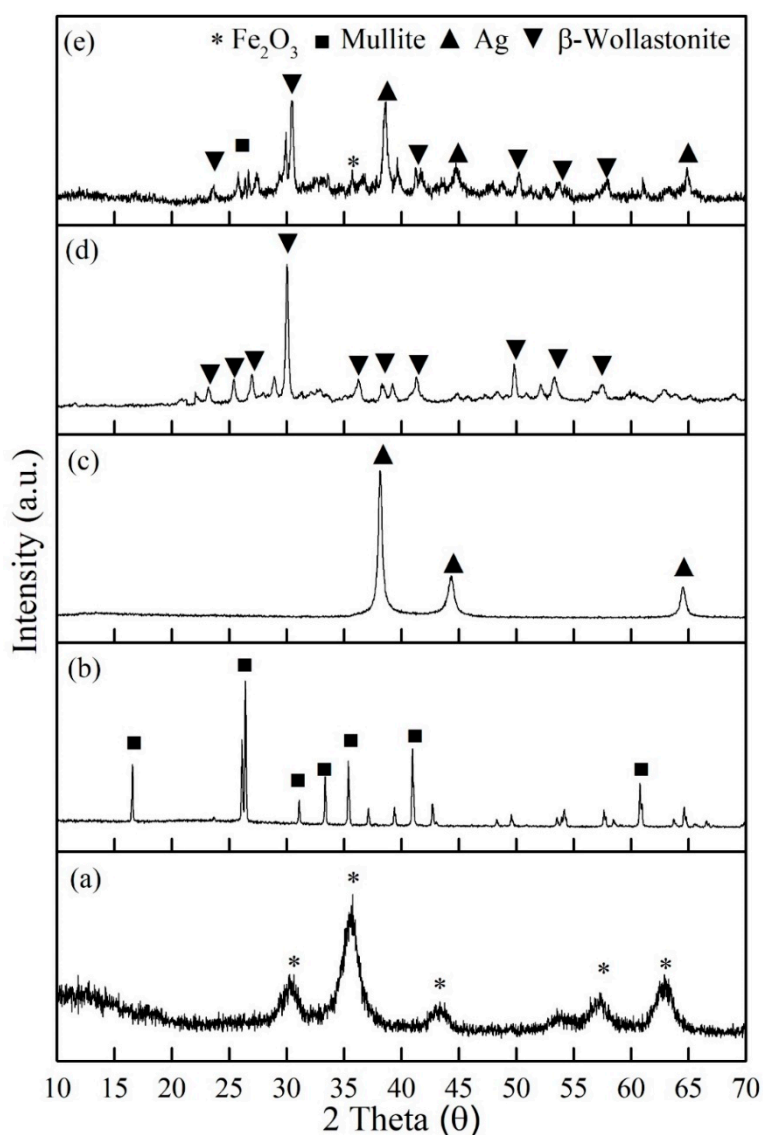


Figure 1. XRD analysis of all the raw materials; (a) maghemite (γ - Fe_2O_3), (b) mullite, (c) silver, (d) β W, and (e) β WMAF composite powders.

The micrograph of the β W and β WMAF discs are presented in Figure 2 and act as a control sample (unsoaked) for bioactivity test. Morphology observation showed that the β W and β WMAF discs show a porous structure (Figure 2a,b). The β W disc image showed that the surface was smooth and exhibited a uniform coral-like shape (Figure 2a), and the EDX spectrum displayed the presence of Ca, Si, O, and P, where the P came from rice husk ash. The surface disc of β WMAF showed a bulky, irregular shape and uneven surface due to many elements, such as mullite, silver, and maghemite, and it was confirmed by the EDX spectrum, which showed the presence of Ca, Si, O, Fe, Ag, Al, and P elements (Figure 2b). Another reason was that the milling process used to prepare the β WMAF mixture may have changed the coral-like microstructure of β W into a bulky, irregular shape with an uneven surface (Figure 2b). The silver, maghemite, and mullite particles are scattered throughout the matrix, with some of them clustered. One of the most critical aspects of successful composite preparation is the uniform distribution of silver, maghemite, and mullite particles.

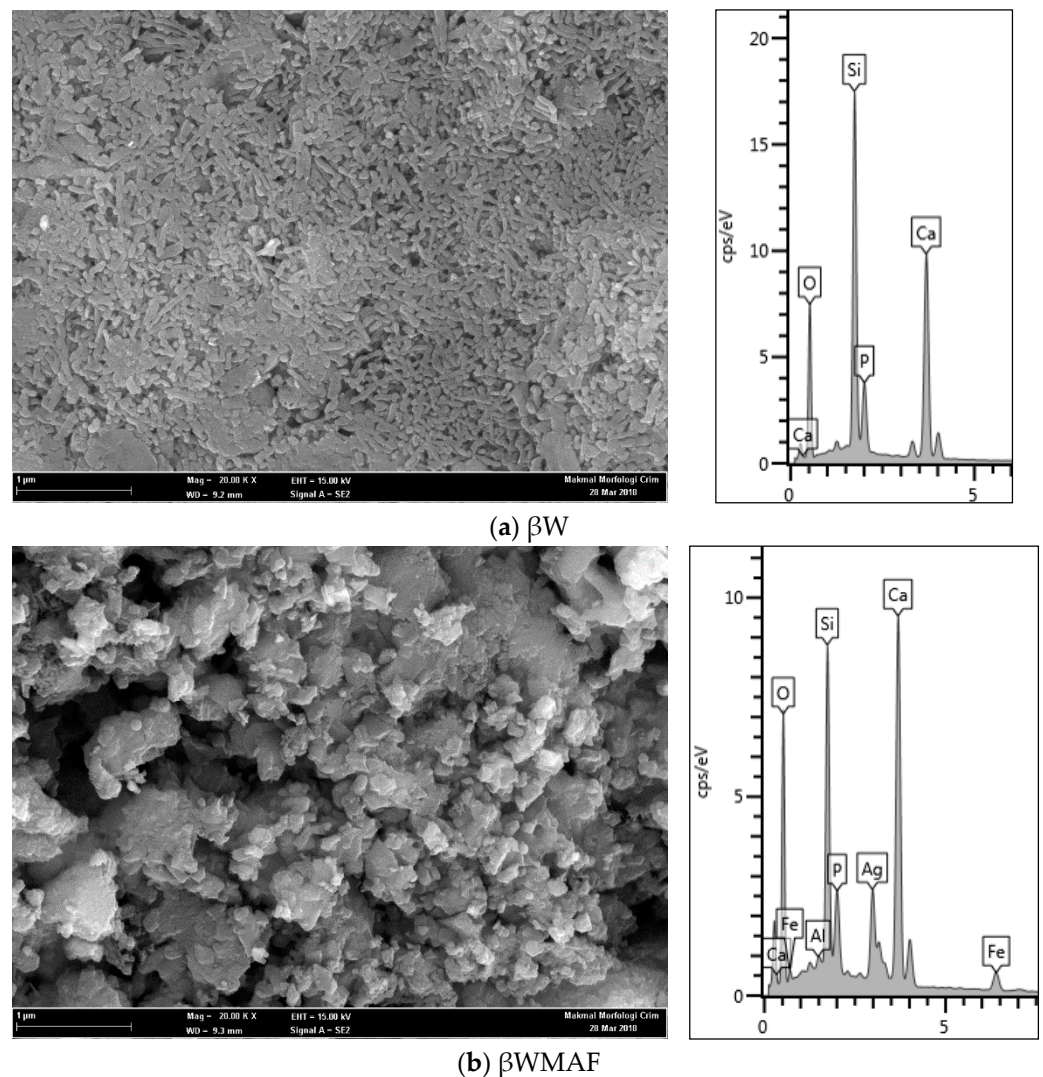


Figure 2. Morphology observation and EDAX spectra of (a) βW and (b) $\beta WMAF$ discs.

3.2. Diametral Tensile Strength (DTS) βW and $\beta WMAF$

The addition of mullite to the $\beta WMAF$ increased the DTS compared to βW . The maximum strength of the βW sample in the absence of reinforcement was 0.69 ± 0.13 MPa. The addition of 20 wt.% mullite as reinforcement to the $\beta WMAF$ increased the strength to 2.39 ± 0.25 MPa, and it was appropriate for cancellous bone implant or scaffold with a compressive strength between 2–12 MPa [47]. Farah et al. obtained the highest DTS value (4.4 ± 0.15 MPa) when using 20 wt.% and the lowest DTS value (2.9 ± 0.15 MPa) when adding 30 wt.% to pseudowollastonite sintered at 1000 °C [39]. Zhang et al. also reported the effects of adding various alumina (0.25, 2, and 5 wt.%) on raising the mechanical properties and low-temperature degradation of yttria-stabilized TZP ceramics for dental implants [41]. As a result, the presence of alumina particles at a concentration of 15% by weight in calcium silicate matrix strength increased the fracture toughness and hardness of calcium silicate [40].

3.3. Magnetic Properties

Magnetization curves of the maghemite ($\gamma\text{-Fe}_2\text{O}_3$), β -wollastonite (βW), and $\beta WMAF$ powders at room temperature are shown in Figure 3. The βW materials had no magnetization and showed a diamagnetic property due to their non-magnetic nature. No hysteresis loop for the βW , due to the B–H relationship, was linear. Simultaneously, the $\beta WMAF$ had a magnetization of 1.731 emu g^{-1} at 25 kOe, because the combined Fe ions formed a

magnetite structure. Similarly, almost no hysteresis loops were found on the curves of the β WMAF, indicating superparamagnetic behavior. Further research needs to investigate β WMAF properties due to the heating ability, specifically, using β WMAF as thermoseeds for hyperthermia treatment of solid cancer tumors under an alternating magnetic field.

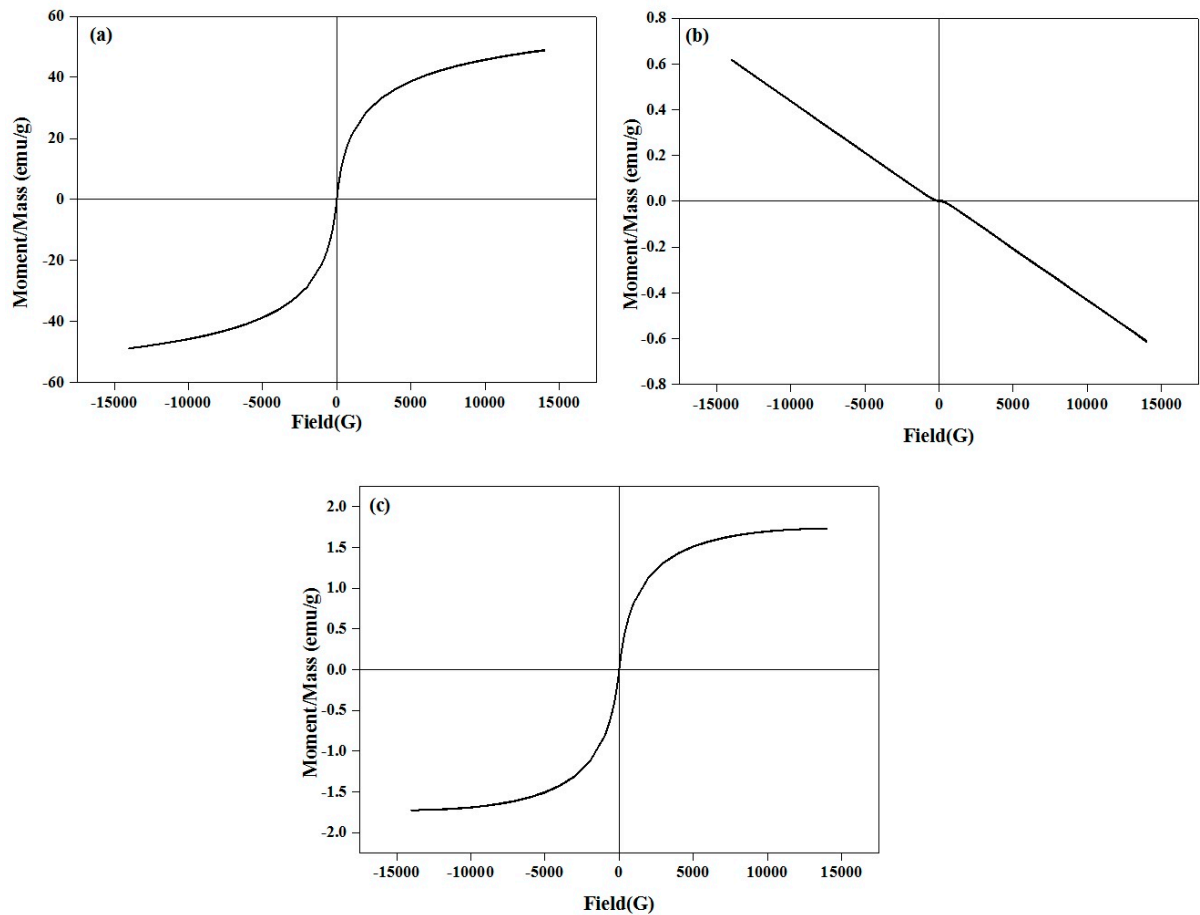


Figure 3. Hysteresis loop of the (a) maghemite (γ -Fe₂O₃), (b) β W, and (c) β WMAF powders.

3.4. In Vitro Bioactivity

Figure 4 shows the XRD diffraction patterns of the β W and β WMAF samples after 14 days of soaking in SBF. The XRD patterns of β W and β WMAF samples before and after soaking showed a sharp peak at $2\theta = 30.0^\circ$, corresponding to the beta-wollastonite (β -CaSiO₃) phase (ICDD no. 00-043-1460), as shown in Figure 4a,b. The resulting XRD trends revealed that the intensity of the β -wollastonite phase in the β W control was reduced after 1 day of soaking, and the calcite phase (CaO) (ICDD no. 00-05-586) was present at 29.3 °C (Figure 4a). The peak intensity of the formed calcite increased dramatically from day 1 to day 7 of soaking and unfortunately disappeared at day 14; this could be attributed to the deposition of amorphous precipitate on the surface of β W. The amorphous precipitate refers to the peak of the hydroxyapatite (HA, ICDD no. 00-09-0302). It was observed as early as day 7; the peak became more apparent on day 14 of the soaking process. However, the intensity for β -wollastonite was still high compared to HA after 14 days of soaking.

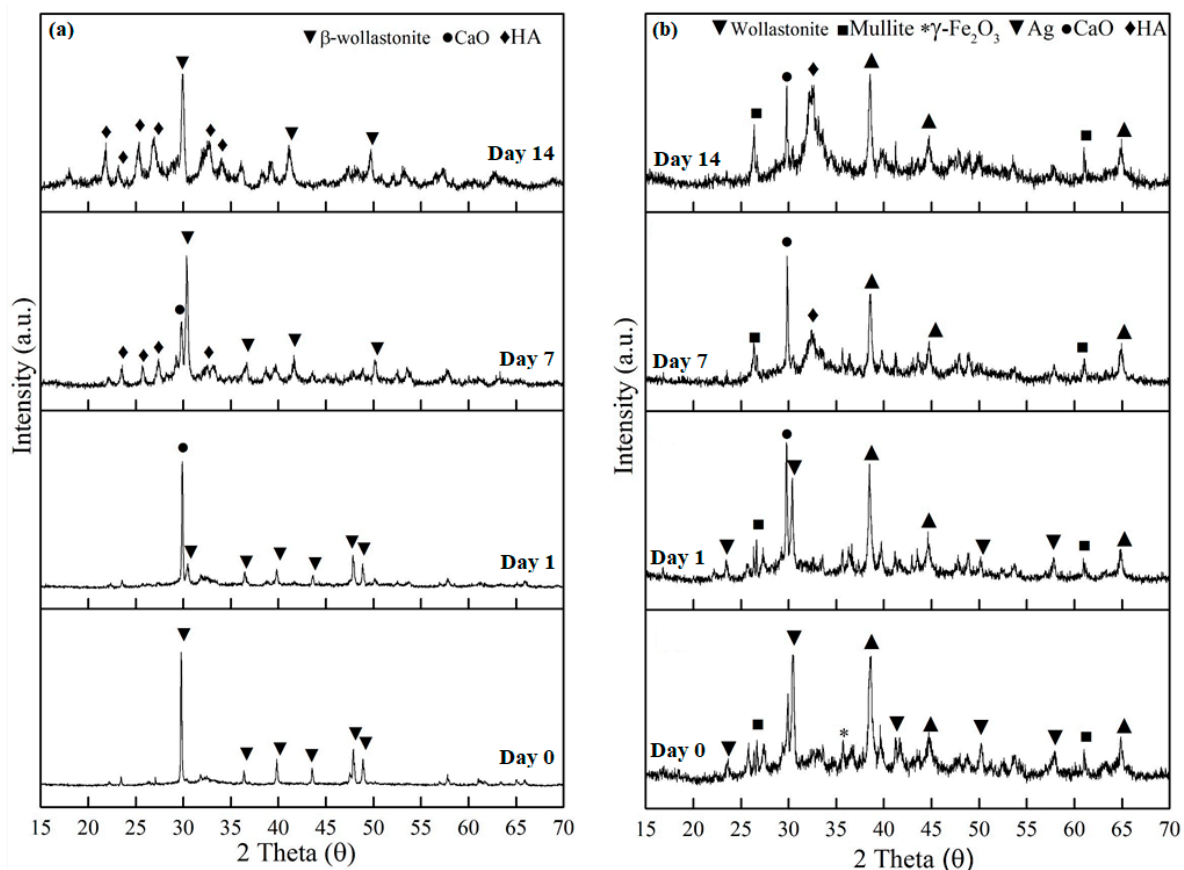
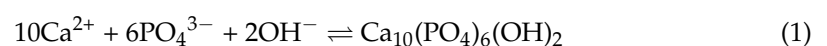


Figure 4. The XRD patterns of the (a) β W and (b) β WMAF before and after soaking until day 14 in an SBF solution.

Meanwhile, for β WMAF, some phases were detected, such as β -wollastonite, mullite, maghemite, and silver, before soaking in the SBF for 14 days (Figure 4b). The β -wollastonite peak intensity at $2\theta = 30.0^\circ$ was decreased and surprisingly disappeared on day 7 of soaking. The calcite peak at $2\theta = 29.3^\circ$ was present after a day of soaking until day 14. Hydroxyapatite (HA) peak was discernible at day 7 of soaking in the SBF compared to the β W sample (Figure 4a). Unpredictably, the intensity peak for calcite and HA was quite the same, and the rest peak of mullite, maghemite, and silver was still there after 14 days of soaking (Figure 4b).

The calcium (Ca^{2+}) and silicon (Si^{4+}) ions released by the samples entered the SBF solution as they were immersed in it. The H^+ ions replaced the Ca^{2+} ions in the samples in the SBF solution as the samples were immersed in the solution, resulting in the formation of silanol (Si-OH) on the surface and an increase in the pH of the SBF solution [48]. The silanol (Si-OH) layer formed on the sample surface aided in forming the hydroxyapatite (HA) phase. The SBF's phosphate (PO_4^{3-}) ions reacted with Ca^{2+} ions in the solution to form the HA phase on the sample [49]. As stated by Sainz et al. [50], this Equation (1) is comparable to the common equation that exists during the HA formation process ($\text{Ca}_{10}(\text{PO}_4)_6(\text{OH})_2$):



According to the XRD patterns, replacing SBF every three days had a significant impact on the formation of apatite phases on the surface of the β W and β WMAF samples because there was an adequate supply of PO_4^{3-} ions from the SBF solution to be mixed with Ca^{2+} ions from the samples to form the apatite layer. In summary, the β WMAF sample was more bioactive than β W, where no β -wollastonite peak was detected up to 14 days of soaking. In this study, apatite formation on the surface of β WMAF was influenced by

maghemite and silver. Some researchers also confirmed the use of silver and maghemite as dopant materials [46,51,52]. Meanwhile, mullite does not help in apatite formation due to its inert properties in nature [51].

Figure 5 depicts the FTIR spectra of β W and β WMAF samples before and after soaking for up to 14 days. As other researchers have discovered, an extensive OH⁻ absorption band at 3600 and 2700 cm⁻¹ and a small water absorption band at 1600 cm⁻¹ can be perceived in these spectra for both samples [35,50]. Before soaking, the absorption band characteristics of β W and β WMAF demonstrated the formation of a β -wollastonite phase dependent on the silicone ion bending bands (Si–O) at 1008.50 and 930.76 cm⁻¹ [40,52]. β -wollastonite phases characterized silicon ion stretching bands (Si–O–Si) at 897.78 and 898.90 cm⁻¹. Carbonate CO₃²⁻ infrared (IR) absorption of β W and β WMAF samples were responsible for the 1419.23 and 1420.03 cm⁻¹ bands. Previous research has shown that the bioactive process began between the 1008.50 and 930.76 cm⁻¹ bands, as evidenced by the presence of non-bridging oxygen-stretching modes [1,29]. These bands regulate the rate of silicate matrix formation, which resulted in the formation of the silanol group at the surface of the β W and β WMAF. The same reaction was observed in the sample soaked for 1 day, as evidenced by the Si ions' decreased strength. This situation indicated the need for Si ions to grow the Si–OH group, which induced apatite formation from day 1 onwards [1]. After soaking for 7 days, the P–O bending band's deep width was observed to be 1021.61 cm⁻¹ for the β WMAF sample, higher than the β W sample, which also occurred in stoichiometric apatite [31]. This finding was supported by XRD data, which showed that β WMAF had a higher apatite formation peak than β W (Figure 4).

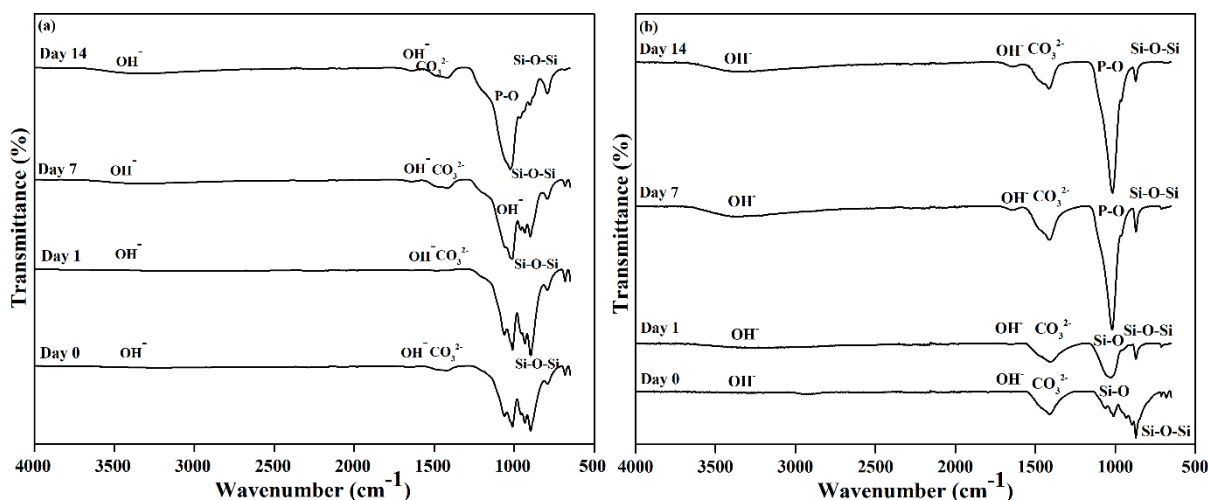


Figure 5. FTIR spectra of the (a) β W and (b) β WMAF before and after soaking in SBF from day 1 until day 14.

Figure 6 depicts the FESEM/EDX analyses of surface apatite after up to 14 days of soaking in SBF for β W and β WMAF. As visualized for day 1, spherical precipitates were observable on the surface of the β W and β WMAF. Similarly, both samples also developed spherules of about 1 μ m in size, showing an apparent inclination to attract apatite precipitates to their surfaces. Up to 7 days of soaking, crystal growth on the spherules surface became more significant for both samples, as shown in Figure 6. Next, for 14 days of soaking, spherules were incorporated to become more significant, and the spherules' shape disappeared in both samples. From day 1 to day 14, soaked samples were SEM/EDX analyzed to confirm that the identified precipitates were apatite formed from an SBF solution. Colfen [50] introduced the surface-directed calcium phosphate mineralization process and observed the improvements in crystal structures in the β W and β WMAF samples that have been soaked for long periods. After soaking the β W and β WMAF samples in SBF, the mechanism began by creating ions such as Si⁴⁺, Ca²⁺, Fe³⁺, Ag⁺, H⁺, OH⁻, and HPO₄²⁻. A day after soaking, the pre-nucleation aggregates in the

arrangement's spherule shape were in balance with the ions in the SBF solution, as revealed in Figure 6a,b; β W and β WMAF samples, respectively. During soaking, pre-nucleation aggregates began to form on the spherules near the surface of the β W and β WMAF, with loose aggregates still in the solution. There was more aggregation, inducing densification at the surface of the spherules of β W and β WMAF. At the surface of the β W and β WMAF, the nucleation of amorphous spherule particles started to occur, and these particles emerged as amorphous calcium phosphate (ACP) on the β W and β WMAF surfaces, respectively (Figure 6a,b). Next, crystallization occurred in the amorphous spherule region, directed by the surface, in the mineralization of calcium phosphate. The Ca/P ratios of the β W and β WMAF immersed surfaces varied from 6.4 to 2.25 and 9.4 to 1.76, respectively, as seen in Figure 7a. Interestingly, the Ca/P ratio decreased significantly within the presence of maghemite and silver due to the variety of ions dissolution, such as Al^{3+} , Fe^{3+} , and Ag^+ in β WMAF. The factor may cause the crystal growth on the spherules surface Ca/P ratio, which was 2.25 (β W) and 1.76 (β WMAF) upon 14 days of immersing (Figure 7a). This value met the amorphous calcium phosphate (ACP) Ca/P ratio, varying from 1.2 to 2.2 [53].

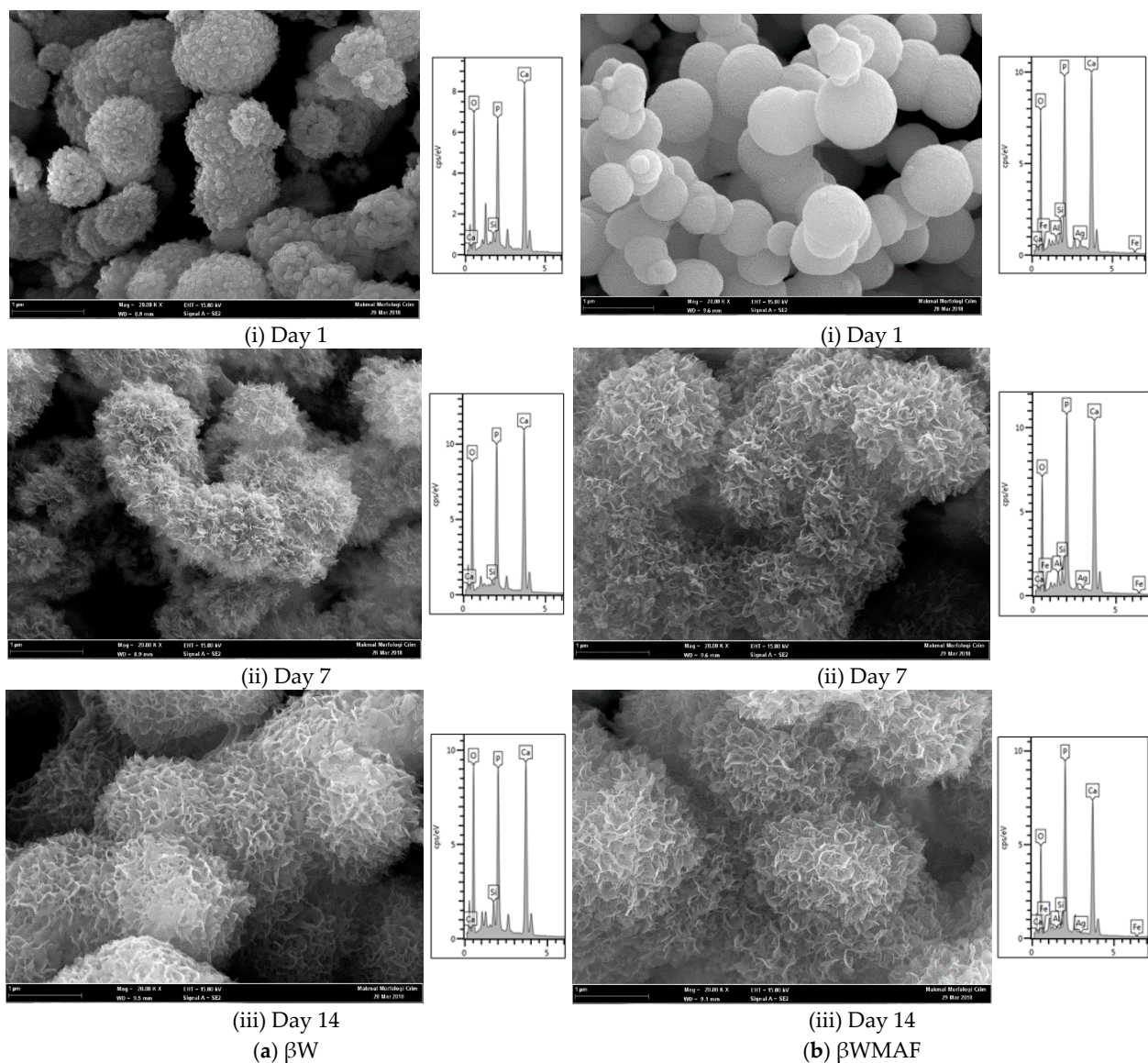


Figure 6. Morphology and elemental analysis of the (a) β W and (b) β WMAF disc sample after soaking in SBF from day 1 until day 14.

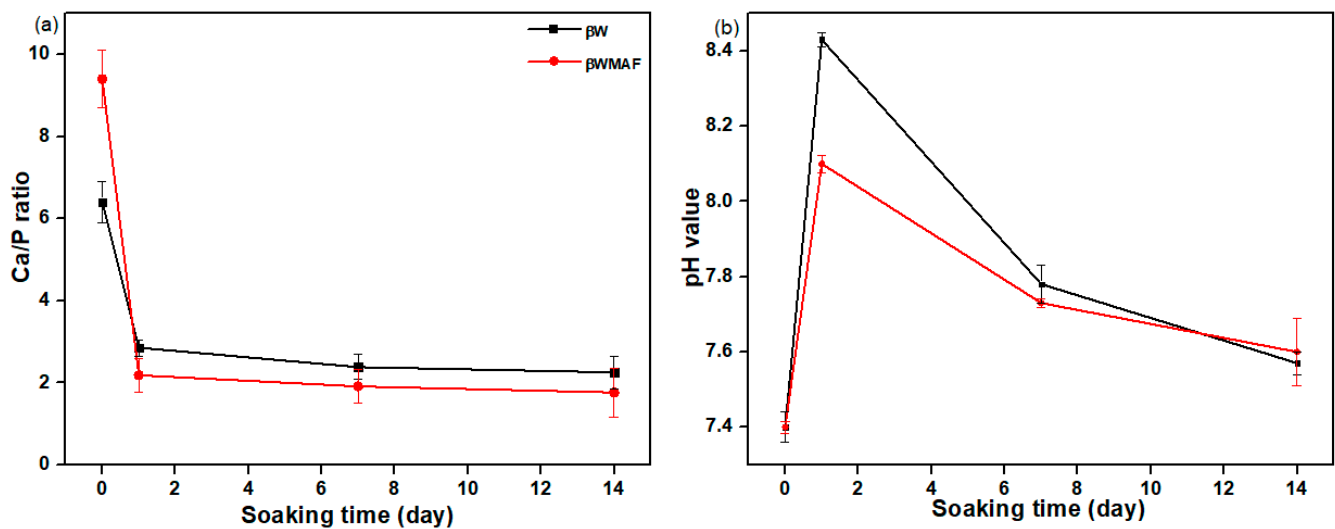


Figure 7. The (a) Ca/P ratio and (b) pH value of β W and β WMAF disc sample before and after soaking in the SBF up to 14 days.

The pH study of β W and β WMAF disc samples suggested an ion exchange process between the sample surface and SBF solution. Changes in the pH of samples in SBF are presented in Figure 7b. A quick increase in the pH solution showed the exchange of ions between β W and β WMAF samples, such as Ca^{2+} , Si^{4+} , Ag^+ , Fe^{2+} , Al^{3+} , with ions from SBF solution, such as OH^- , PO_4^{3-} , and Na^+ . The pH value for β W samples from day 1 soaking was 7.4 up to 8.10 and decreased to 7.60 and, for the β WMAF sample, from 7.4 up to 8.43 and decreased to 7.62 after 14 days of soaking. The pH of the solution changed in a small range for β W and β WMAF samples, which indicated that samples were chemically stable in SBF solution and did not show any acidic nature in SBF. Instead, ion release would also alter biomaterial pH, influencing cell growth and osseointegration [54].

3.5. Ca, P, Fe, and Ag Release in SBF Solution

Figure 8 shows the release of Ca, Si, P, Fe, and Ag ions for 1, 7, and 14 days in the SBF solution being calculated using ICP-MS. Therefore, the release of Ca, Si, P, Fe, and Ag ions from β WMAF in the SBF solution was examined. As shown in Figure 9, except for the P ion, the drastic release of increased Ca, Si, Fe, and Ag ions was observed, with the rise in immersing time decreased. Parallel Ca and Si ion concentrations increased with increasing Fe substitution, which may be attributable to Fe ions having more Si and O network bonds than Ca ions, leading to a more robust β WMAF network. After the next 7 days, Ca, Si, Fe, and Ag's dissolution rate slowed until day 14. After 14 days, the total Ca, Si, Fe, Ag, and P in the β WMAF were 265.81, 74.06, 1.18, 2.87, and 0.033 ppm, respectively.

In comparison, the Ag ion release peaked around days 2–6, and the decrease of Ag ion was subsequently observed after day 7. Ag ions' complete release during the initial process could provide successful antibacterial activity, avoiding infections linked to the surgical site. Ag's minimum bacterial concentration is 0.1 ppm, so this total of released Ag ions was sufficiently large to prevent bacteria growth.

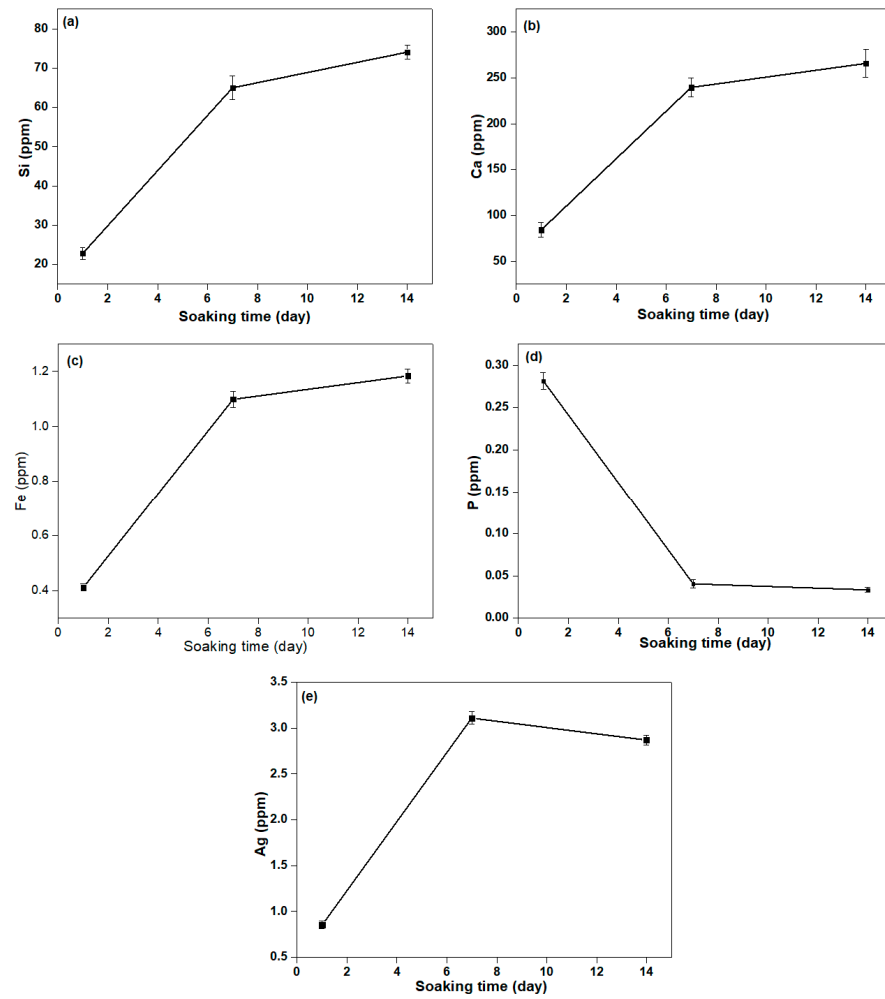


Figure 8. The concentration of (a) Si, (b) Ca, (c) Fe, (d) P, and (e) Ag ion release from β WMAF samples in the SBF solution for 1, 7, and 14 days.

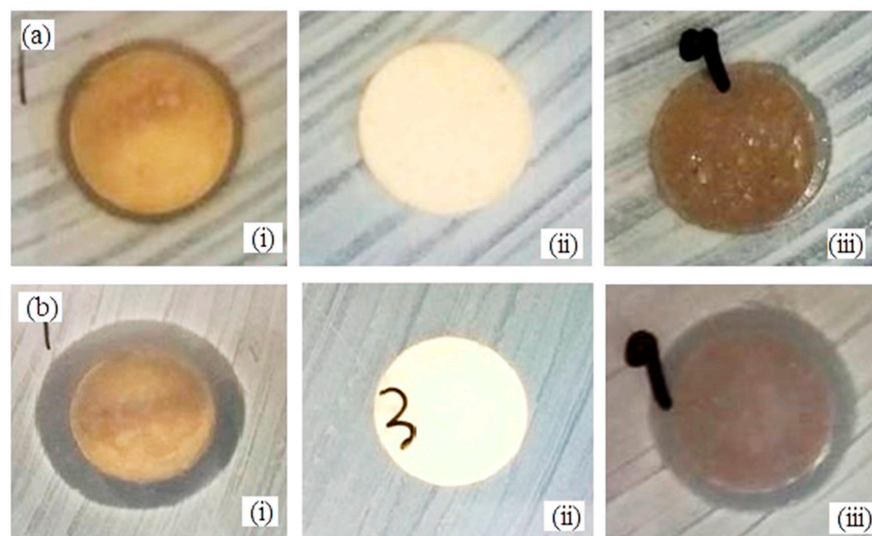


Figure 9. Antimicrobial activity by disc diffusion test of (i) Ag (control sample), (ii) β W and (iii) β WMAF disc for (a) *E. coli* and (b) *S. aureus*.

3.6. Antimicrobial Study

In order to investigate the antimicrobial activity of β WMAF (12 mm diameter disc), the disc diffusion method was applied by using *E. coli* and *S. aureus* bacteria as test culture. The antibacterial activity can be observed from the clear zone of bacterial inhibition area around the test disk, as seen in Figure 9. Figure 10 shows the zone of inhibition (ZOI) measured by the disc diffusion test as a function of Ag for a β W and β WMAF disc for *E. coli* and *S. aureus*. A surprisingly good inhibition zone was observed for β WMAF on two different bacteria (Figure 9). The inhibition zone (ZOI) for *E. coli* was estimated at 14.1 mm for β WMAF and Ag, as seen in Figure 10. For *S. aureus*, Ag showed a higher ZOI than β WMAF, with readings of 17.0 mm and 15.8 mm, respectively, as described in Figure 10. The observations also found that pathogenic inhibition was seen less in *S. aureus* than in *E. coli* because of a generous thicker peptidoglycan layer, being characteristic of *S. aureus*. Several studies showed that *S. aureus* is more resistant to antimicrobial compounds than *E. coli* [55].

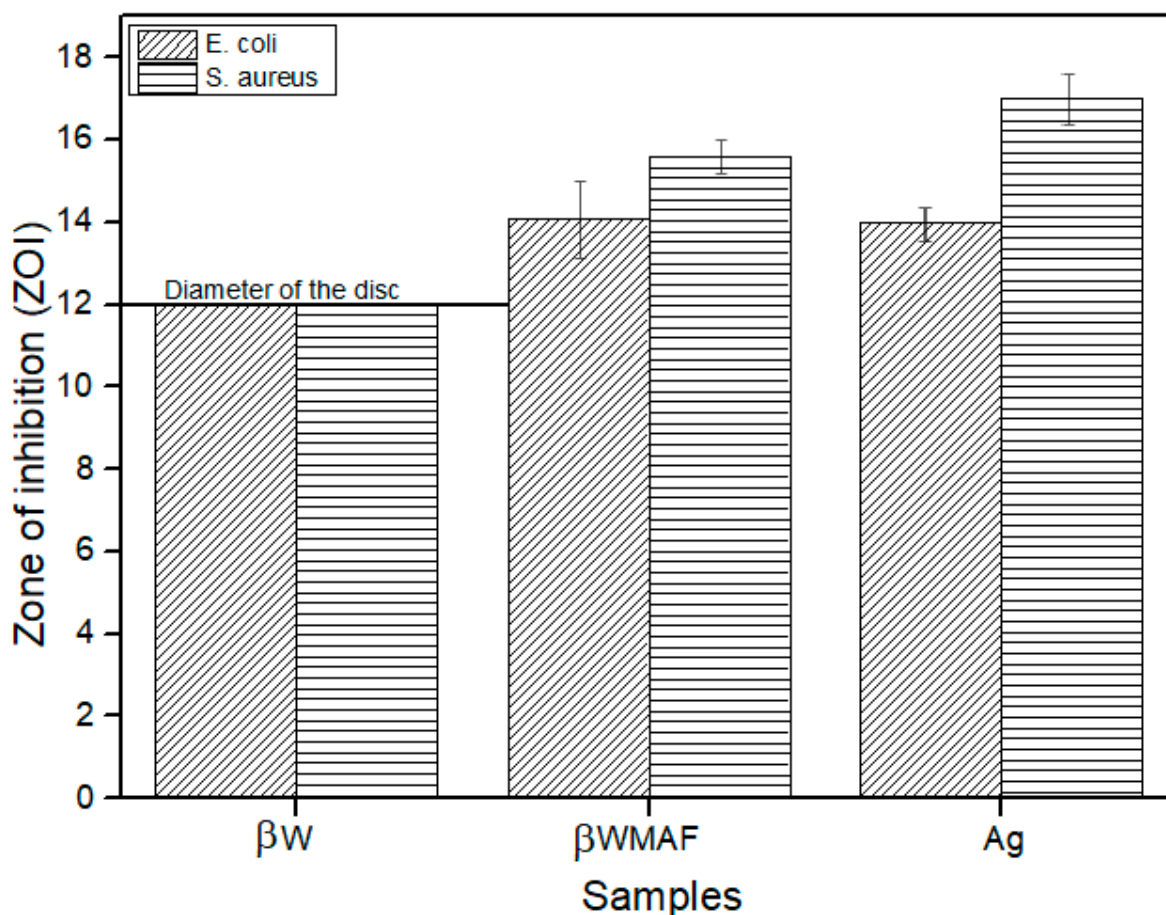


Figure 10. Zone of inhibition (ZOI) of the β W (negative control), β WMAF, and Ag (positive control) disc samples after 24 h.

However, no inhibition zones were found on β W, implying that β W lacked bactericidal or bacteriostatic activity. The most common cause of implantation infections that resulted in implant failure was bacterial adhesion to the implant material. Several studies on metal ion-based modification by loading antibacterial agents such as Cu, Ag, and Zn were published to improve silicate bioceramic antimicrobial activity [56]. This ion-based alteration could also influence the toxicity and degree of structural integrity. Therefore, the currently prepared β W using calcined limestone and rice husk ash demonstrated possible antibacterial agent doping on microbial growth inhibition, close to other researchers' findings [57,58]. The mechanism for the antimicrobial action of silver ions is not ade-

quately understood. However, the prepared β WMAF may also be a possible candidate for biomedical applications.

4. Conclusions

The magnetism, bioactivity, and antibacterial activity of β W and β WMAF synthesized from locally available materials, such as rice husk ash (RHA) and limestone ash, were investigated. The inclusion of 20 wt.% mullite into the β W increased the compressive strength up to 200%, which is appropriate for the cancellous bone application; moreover, adding 5 wt.% Ag into the β W produced an excellent antibacterial property against *E. coli* and *S. aureus*. In vitro bioactivity findings revealed that apatite crystals were close-packed and fragile, with a quicker growth rate on β WMAF than on β W. The most crucial antimicrobial analysis indicated that β WMAF samples were antibacterial against *E. coli* and *S. aureus*. Furthermore, cytotoxic assays of the β W and β WMAF must be critically characterized. Another issue is creating a β WMAF bioceramic composite with strong antibacterial characteristics and low cytotoxic risk. As a result, further changes to the fabrication to improve crystallinity and reduce the dissolution of Fe and Ag during the early stage may render the bioceramics composite non-toxic to human cells. As a result, the current study findings provide new insights into the first step of future complex work to fabricate magnetic antibacterial β -wollastonite bioceramic composite scaffolds for bone regeneration. Development of calcium and silica-based material biowaste further improves the significant advantages in biomaterial applications.

Author Contributions: Conceptualization, H.I. and M.A.A.H.; methodology, H.I., F.A.A.A., M.A.A.; validation, H.B., H.M., Z.Z.; formal analysis, H.I.; investigation, F.A.A.A., M.A.A.; resources, H.I.; data curation, H.I.; writing—original draft preparation, H.I.; writing—review and editing, H.I., M.A.A.; visualization, Z.Z.; supervision, M.A.A.H.; project administration, Z.Z.; funding acquisition, M.A.A.H. All authors have read and agreed to the published version of the manuscript.

Funding: This research was funded by Ministry of Higher Education of Malaysia, grant number DCP-2017-0011/1.

Institutional Review Board Statement: Not applicable.

Informed Consent Statement: Not applicable.

Data Availability Statement: Not applicable.

Acknowledgments: The authors would like to express their gratitude to Roslinda Shamsudin for her valuable and helpful recommendations in preparing and developing this research work. The authors would also like to thank the Faculty of Science and Technology and CRIM, Universiti Kebangsaan Malaysia and University Sains Malaysia.

Conflicts of Interest: The authors declare no conflict of interest.

References

1. Gandolfi, M.G.; Ciapetti, G.; Taddei, P.; Perut, F.; Tinti, A.; Cardoso, M.V.; Van Meerbeek, B.; Prati, C. Apatite formation on bioactive calcium-silicate cements for dentistry affects surface topography and human marrow stromal cells proliferation. *Dent. Mater.* **2010**, *26*, 974–992. [[CrossRef](#)]
2. Xie, Y.; Li, H.; Zhang, C.; Gu, X.; Zheng, X.; Huang, L. Graphene-reinforced calcium silicate coatings for load-bearing implants. *Biomed. Mater.* **2014**, *9*, 025009. [[CrossRef](#)]
3. Sathain, A.; Monvisade, P.; Siriphannon, P. Bioactive alginate / carrageenan/calcium silicate porous scaffolds for bone tissue engineering. *Mater. Today Commun.* **2021**, *26*, 102165. [[CrossRef](#)]
4. Zhang, Z.; Shao, H.; Lin, T.; Zhang, Y.; He, J.; Wang, L. 3D gel printing of porous calcium silicate scaffold for bone tissue engineering. *J. Mater. Sci.* **2019**, *54*, 10430–10436. [[CrossRef](#)]
5. Feng, P.; Wei, P.; Li, P.; Gao, C.; Shuai, C.; Peng, S. Calcium silicate ceramic scaffolds toughened with hydroxyapatite whiskers for bone tissue engineering. *Mater. Charact.* **2014**, *97*, 47–56. [[CrossRef](#)]
6. Demiryürek, E.Ö.; Özyürek, T.; Gülhan, T. Evaluation of antibacterial and antifungal activity of calcium silicate based retrograde filling materials. *Int. J. Appl. Dent. Sci.* **2016**, *2*, 85–88.
7. Ridzwan, H.J.M.; Shamsudin, R.; Ismail, H.; Yusof, M.R.; Hamid, M.A.A.; Awang, R.B. Compressive strength and magnetic properties of calcium silicate-zirconia-iron (III) oxide composite cements. *AIP Conf. Proc.* **2018**, *1940*, 1–7. [[CrossRef](#)]

8. Wu, C.; Ramaswamy, Y.; Kwik, D.; Zreiqat, H. The effect of strontium incorporation into CaSiO₃ ceramics on their physical and biological properties. *Biomaterials* **2007**, *28*, 3171–3181. [[CrossRef](#)]
9. Ballo, M.K.S.; Rtimi, S.; Pulgarin, C.; Hopf, N.; Berthet, A.; Kiwi, J.; Moreillon, P.; Entenza, J.M.; Bizzini, A. In Vitro and In Vivo effectiveness of an innovative silver-copper nanoparticle coating of catheters to prevent methicillin-resistant *Staphylococcus aureus* infection. *Antimicrob. Agents Chemother.* **2016**, *60*, 5349–5356. [[CrossRef](#)]
10. Ewais, E.M.M.; Amin, A.M.M.; Ahmed, Y.M.Z.; Ashor, E.A.; Hess, U.; Rezwan, K. Combined effect of magnesia and zirconia on the bioactivity of calcium silicate ceramics at C/S ratio less than unity. *Mater. Sci. Eng. C* **2017**, *70*, 155–160. [[CrossRef](#)]
11. Ortega-Lara, W.; Cortés-Hernández, D.A.; Best, S.; Brooks, R.; Bretado-Aragón, L.; Rentería-Zamarrón, D. In vitro bioactivity of wollastonite-titania materials obtained by sol-gel method or solid state reaction. *J. Sol-Gel Sci. Technol.* **2008**, *48*, 362–368. [[CrossRef](#)]
12. No, Y.J.; Li, J.J.; Zreiqat, H. Doped calcium silicate ceramics: A new class of candidates for synthetic bone substitutes. *Materials* **2017**, *10*, 153. [[CrossRef](#)]
13. Mohammadi, H.; Hafezi, M.; Nezafati, N.; Heasarki, S.; Nadernezhad, A.; Ghazanfari, S.M.H.; Sepantafar, M. Bioinorganics in bioactive calcium silicate ceramics for bone tissue repair: Bioactivity and biological properties. *J. Ceram. Sci. Technol.* **2014**, *5*, 1–12. [[CrossRef](#)]
14. Civantos, A.; Martínez-Campos, E.; Mónica, V.; Elvira, C.; Gallardo, A.; Abarrategi, A. Titanium coatings and surface modifications: Towards clinically useful bioactive implants. *ACS Biomater. Sci. Eng.* **2017**, *3*, 1245–1261. [[CrossRef](#)]
15. Patil, U.S.; Adireddy, S.; Jaiswal, A.; Mandava, S.; Lee, B.R.; Chrisey, D.B. In vitro/in vivo toxicity evaluation and quantification of iron oxide nanoparticles. *Int. J. Mol. Sci.* **2015**, *16*, 24417–24450. [[CrossRef](#)]
16. Priyadarsini, S.; Mukherjee, S.; Mishra, M. Nanoparticles used in dentistry: A review. *J. Oral Biol. Craniofacial Res.* **2018**, *8*, 840–843. [[CrossRef](#)] [[PubMed](#)]
17. Auffan, M.; Decome, L.; Rose, J.; Orsiere, T.; De Meo, M.; Briois, V.; Chaneac, C.; Olivi, L.; Berge-LeFranc, J.L.; Botta, A.; et al. In vitro interactions between DMSA-coated maghemite nanoparticles and human fibroblasts: A physicochemical and cytogenotoxic study. *Environ. Sci. Technol.* **2006**, *40*, 4367–4373. [[CrossRef](#)]
18. Kesse, X.; Adam, A.; Begin-Colin, S.; Mertz, D.; Larquet, E.; Gacoin, T.; Maurin, I.; Vichery, C.; Nedelec, J. Elaboration of superparamagnetic and bioactive multicore-shell nanoparticles (γ -Fe₂O₃ @ SiO₂-CaO): A promising material for bone cancer treatment. *ACS Appl. Mater. Interfaces* **2020**, *12*, 47820–47830. [[CrossRef](#)]
19. Corrêa, J.M.; Mori, M.; Sanches, H.L.; Cruz, A.D.D.; Poiate, E.; Poiate, I.A.V.P. Silver Nanoparticles in Dental Biomaterials. *Int. J. Biomater.* **2015**, *2015*, 485275. [[CrossRef](#)]
20. Konop, M.; Damps, T.; Misicka, A.; Rudnicka, L. Certain Aspects of Silver and Silver Nanoparticles in Wound Care: A Minireview. *J. Nanomater.* **2016**, *2016*, 7614753. [[CrossRef](#)]
21. Brunner, T.J.; Wick, P.; Manser, P.; Spohn, P.; Grass, N.; Limbach, L.K.; Bruinink, A.; Stark, W.J. In Vitro Cytotoxicity of Oxide Nanoparticles: Comparison to Asbestos, Silica, and the Effect of Particle Solubility. *Environ. Sci. Technol.* **2006**, *40*, 4374–4381. [[CrossRef](#)]
22. Soto, K.; Garza, K.M.; Murr, L.E. Cytotoxic effects of aggregated nanomaterials. *Acta Biomater.* **2007**, *3*, 351–358. [[CrossRef](#)] [[PubMed](#)]
23. Pisanic, T.R.; Blackwell, J.D.; Shubayev, V.I.; Fiñones, R.R.; Jin, S. Nanotoxicity of iron oxide nanoparticle internalization in growing neurons. *Biomaterials* **2007**, *28*, 2572–2581. [[CrossRef](#)] [[PubMed](#)]
24. Lansdown, A.B.G. Silver in Health Care: Antimicrobial Effects and Safety in Use. *Curr. Probl. Dermatol.* **2006**, *33*, 17–34. [[PubMed](#)]
25. Randall, C.P.; Gupta, A.; Jackson, N.; Busse, D.; Neill, A.J.O. Silver resistance in Gram-negative bacteria: A dissection of endogenous and exogenous mechanisms. *J. Antimicrob. Chemother.* **2015**, *70*, 1037–1046. [[CrossRef](#)]
26. Kedziora, A.; Speruda, M.; Krzyzewska, E.; Rybka, J.; Łukowiak, A.; Bugla-Płoskonska, G. Similarities and Differences between Silver Ions and Silver in Nanoforms as Antibacterial Agents. *Int. J. Mol. Sci.* **2018**, *19*, 444. [[CrossRef](#)]
27. Stensberg, M.C.; Wei, Q.; Mclamore, E.S.; Marshall, D. Toxicological studies on silver nanoparticles. *Nanomedicine* **2012**, *6*, 879–898. [[CrossRef](#)]
28. Singh, S.P.; Bhargava, D.C.S.; Dubey, D.V.; Mishra, A.; Singh, Y. Silver nanoparticles: Biomedical applications, toxicity, and safety issues. *Int. J. Res. Pharm. Pharm. Sci.* **2017**, *2*, 01–10.
29. Huh, A.J.; Kwon, Y.J. “Nanoantibiotics”: A new paradigm for treating infectious diseases using nanomaterials in the antibiotics resistant era. *J. Control Release* **2011**, *156*, 128–145. [[CrossRef](#)]
30. Ciobanu, C.S.; Iconaru, S.L.; Chifiriuc, M.C.; Costescu, A.; Coustumer, P.L.; Predoi, D. Synthesis and antimicrobial activity of silver-doped hydroxyapatite nanoparticles. *Biomed. Res. Int.* **2013**, *2013*, 916218. [[CrossRef](#)]
31. Kolmas, J.; Groszyk, E.; Kwiatkowska-Różycka, D. Substituted hydroxyapatites with antibacterial properties. *Biomed Res. Int.* **2014**, *2014*, 178123. [[CrossRef](#)]
32. Barros, J.; Grenho, L.; Fontenente, S.; Manuel, C.M.; Nunes, O.C.; Melo, L.F.; Monteiro, F.J.; Ferraz, M.P. *S. aureus* and *E. coli* dual-species biofilms on nanohydroxyapatite loaded with CHX or ZnO nanoparticles. *J. Biomed. Mater. Res. A* **2017**, *105*, 491–497. [[CrossRef](#)] [[PubMed](#)]
33. El-Nahrawy, A.M.; Ali, A.I.; Hammad, A.B.A.; Youssef, A.M. Influences of Ag-NPs doping chitosan/calcium silicate nanocomposites for optical and antibacterial activity. *Int. J. Biol. Macromol.* **2016**, *93*, 267–275. [[CrossRef](#)]

34. Azam, F.A.A.; Shamsudin, R.; Ng, M.H.; Ahmad, A.; Akbar, M.A.M.; Rashidbenam, Z. Silver-doped pseudowollastonite synthesized from rice husk ash: Antimicrobial evaluation, bioactivity and cytotoxic effects on human mesenchymal stem cells. *Ceram. Int.* **2018**, *44*, 11381–11389. [[CrossRef](#)]
35. Abas, A.; El, A.; El-bassyouni, G.; Hamzawy, E.M.A. CuO Doped Wollastonite Clusters for Some Anti-microbial and Anti-fungi Applications. *Der Pharm. Lett.* **2018**, *10*, 42–54.
36. Kalaivani, S.; Singh, R.K.; Ganesan, V.; Kannan, S. Effect of copper (Cu^{2+}) inclusion on the bioactivity and antibacterial behavior of calcium silicate coatings on titanium metal. *J. Mater. Chem. B* **2014**, *2*, 846–858. [[CrossRef](#)]
37. Lohbauer, U.; Jell, G.; Saravanapavan, P.; Jones, J.R.; Hench, L.L. Indirect cytotoxicity evaluation of silver doped bioglass Ag-S70C30 on human primary keratinocytes. *Key Eng. Mater.* **2005**, *284–286*, 431–434. [[CrossRef](#)]
38. Shi, C.; Gao, J.; Wang, M.; Fu, J.; Wang, D.; Zhu, Y.; Ag, U. Ultra-trace silver-doped hydroxyapatite with non-cytotoxicity and effective antibacterial activity. *Mater. Sci. Eng. C* **2015**, *55*, 497–505. [[CrossRef](#)] [[PubMed](#)]
39. Azam, F.A.A.; Shamsudin, R.; Ng, M.H.; Zainuddin, Z.; Hamid, M.A.A.; Rashid, R.A. Mechanical and Bioactive Properties of Mullite Reinforced Pseudowollastonite Biocomposite. *Sains Malays.* **2018**, *47*, 2141–2149. [[CrossRef](#)]
40. Ismail, H.; Shamsudin, R.; Hamid, M.A.A. Effect of autoclaving and sintering on the formation of β -wollastonite. *Mater. Sci. Eng. C* **2016**, *58*, 1077–1081. [[CrossRef](#)]
41. Shamsudin, R.; Ismail, H.; Hamid, M.A.A. The Suitability of Rice Straw Ash as a Precursor for Synthesizing β -Wollastonite. *Mater. Sci. Forum* **2016**, *846*, 216–222. [[CrossRef](#)]
42. Scapin, M.; Peroni, L.; Avalle, M. Dynamic Brazilian Test for Mechanical Characterization of Ceramic Ballistic Protection. *Shock Vib.* **2017**, *2017*, 7485856. [[CrossRef](#)]
43. Swab, J.; Quinn, G.D. Fractographic Analysis of Ceramic Materials Tested Using the Diametral Compression Test In Ceramic Materials and Components for Engines. 1970. Available online: <https://www.nist.gov/publications/fractographic-analysis-ceramic-materials-tested-using-diametral-compression-test> (accessed on 15 June 2021).
44. Ha, S.; Yang, J.; Lee, J.; Han, J.; Kim, S. Comparison of polymer-based temporary crown and fixed partial denture materials by diametral tensile strength. *J. Adv. Prosthodont* **2010**, *2*, 14–17. [[CrossRef](#)] [[PubMed](#)]
45. Kokubo, T.; Takadama, H. How useful is SBF in predicting in vivo bone bioactivity? *Biomaterials* **2006**, *27*, 2907–2915. [[CrossRef](#)]
46. Zhang, J.; Zhu, Y.; Li, J.; Zhu, M.; Tao, C.; Hanagata, N. Preparation and characterization of multifunctional magnetic mesoporous calcium silicate materials. *Sci. Technol. Adv. Mater.* **2013**, *14*, 055009. [[CrossRef](#)] [[PubMed](#)]
47. Amin, A.M.M.; Ewais, E.M.M. Bioceramic Scaffolds Bioceramic Scaffolds-Materials. In *Scaffolds in Tissue Engineering Materials, Technologies and Clinical Applications*; IntechOpen: London, UK, 2017.
48. Lin, M.; Chen, C.; Wu, L.; Ding, S. Enhanced antibacterial activity of calcium silicate-based hybrid cements for bone repair. *Mater. Sci. Eng. C* **2020**, *110*, 110727. [[CrossRef](#)] [[PubMed](#)]
49. Magallanes-Perdomo, M.; Luklinska, Z.B.; Aza, A.H.D.; Carrodegua, R.G.; Aza, S.D.; Pena, P. Bone-like forming ability of apatite—Wollastonite glass ceramic. *J. Eur. Ceram. Soc.* **2011**, *31*, 1549–1561. [[CrossRef](#)]
50. Sainz, M.A.; Pena, P.; Serena, S.; Caballero, A. Influence of design on bioactivity of novel CaSiO_3 - $\text{CaMg}(\text{SiO}_3)_2$ bioceramics: In vitro simulated body fluid test and thermodynamic simulation. *Acta Biomater.* **2010**, *6*, 2797–2807. [[CrossRef](#)] [[PubMed](#)]
51. Fernandes, L.; Carvalho, R.A.D.; Amaral, A.C.; Pecoraro, E.; Salomão, R.; Trovatti, E. Mullite cytotoxicity and cell adhesion studies. *J. Mater. Res. Technol.* **2019**, *8*, 2565–2572. [[CrossRef](#)]
52. Shamsudin, R.; Azam, F.A.A.; Hamid, M.A.A.; Ismail, H. Bioactivity and cell compatibility of β -wollastonite derived from rice husk ash and limestone. *Materials* **2017**, *10*, 1188. [[CrossRef](#)]
53. Dorozhkin, S. Calcium Orthophosphate-Based Bioceramics. *Materials* **2013**, *6*, 3840–3942. [[CrossRef](#)]
54. Jebahi, S.; Oudadesse, H.; Wers, E.; Elleuch, J.; Elfekih, H.; Keskes, H.; Vuong, X. Effect of pH and Ionic Exchange on the Reactivity of Bioglass /Chitosan Composites Used as a Bone Graft Substitute, International Journal of Chemical, Nuclear. *Mater. Metall. Eng.* **2013**, *7*, 5143–5148.
55. Shahverdi, A.R.; Fakhimi, A.; Shahverdi, H.R.; Minaian, S. Synthesis and effect of silver nanoparticles on the antibacterial activity of different antibiotics against Staphylococcus aureus and Escherichia coli, Nanomedicine Nanotechnology. *Biol. Med.* **2007**, *3*, 168–171. [[CrossRef](#)]
56. Schatkoski, V.M.; Larissa, T.; Rossi, B.; Menezes, C.D.; Pereira, R.M.; Rodrigues, K.F.; Morais, D.; Thim, G.P.; Guimar, R. Current advances concerning the most cited metal ions doped bioceramics and silicate-based bioactive glasses for bone tissue engineering. *Ceramics International* **2020**, *47*, 2999–3012. [[CrossRef](#)]
57. Palakurthy, S.; Azeem, P.A.; Reddy, K.V. In vitro evaluation of silver doped wollastonite synthesized from natural waste for biomedical applications. *Ceram. Int.* **2019**, *45*, 25044–25051. [[CrossRef](#)]
58. Palakurthy, S.; Azeem, P.A.; Reddy, K.V.; Penugurti, V.; Manavathi, B. A comparative study on in vitro behavior of calcium silicate ceramics synthesized from biowaste resources. *J. Am. Ceram. Soc.* **2020**, *103*, 933–943. [[CrossRef](#)]